CHARACTERIZATION OF ANTERIOR CEREBRAL ARTERY BLOOD FLOW IN RESTING STATE BY USING TRANSCRANIAL DOPPLER RECORDINGS

by

Hanrui Huang

B.S. in Electrical Engineering, University of Pittsburgh, 2012

Submitted to the Graduate Faculty of

the Swanson School of Engineering in partial fulfillment

of the requirements for the degree of

Master of Science

University of Pittsburgh

2013

UNIVERSITY OF PITTSBURGH

SWANSON SCHOOL OF ENGINEERING

This thesis was presented

by

Hanrui Huang

It was defended on

March 25, 2013

and approved by

Ervin Sejdić, PhD, Assistant Professor, Department of Electrical and Computer Engineering

Zhi-Hong Mao, PhD, Associate Professor, Department of Electrical and Computer Engineering

Luis F. Chaparro, PhD, Associate Professor, Department of Electrical and Computer Engineering

Thesis Advisor: Ervin Sejdić, PhD, Assistant Professor, Department of Electrical and Computer Engineering

CHARACTERIZATION OF ANTERIOR CEREBRAL ARTERY BLOOD FLOW IN RESTING STATE BY USING TRANSCRANIAL DOPPLER RECORDINGS

Hanrui Huang, M.S.

University of Pittsburgh, 2013

Transcranial Doppler (TCD) recordings are used to monitor cerebral blood flow in main cerebral arteries. The resting state is usually characterized by using the mean velocity or the maximum Doppler shift frequency (an envelope signal) by insonating the middle cerebral arteries (MCAs). In this study, we characterized the cerebral blood flow in the anterior cerebral arteries (ACAs). We analyzed both the envelope signals and the raw signals obtained from bilateral insonation. We recruited 20 healthy subjects and conducted the data acquisition for 15 minutes. Features were extracted from the time domain, the frequency domain and the time-frequency domain. The results showed that gender-based statistical difference exists in the frequency domain and the time-frequency domain. However, no handedness effect was found. In the time domain, the information-theoretic features showed that the mutual dependence is higher in raw signals than in envelope signals. Finally, we concluded that insonating the ACA will serve as a complement of the MCA studies. Additionally, the investigation of the raw signals provided us with additional information that is not otherwise available from the envelope signals. The direct TCD raw-data utilization is therefore validated as a valuable resting-state characterization method.

Keywords: Transcrannial Doppler, anterior cerebral artery, resting-state characteristics.

TABLE OF CONTENTS

LIST OF TABLES

LIST OF FIGURES

PREFACE

I would have not finished this thesis without the support of my family who have always been there for me whenever I need their encouragement which is a great source of strength and inspiration. They have given me endless love that keeps me empowered.

I would like to express the deepest gratitude and greatest appreciation to all participants who have supported me throughout the data collection. The research project would not have been possible without their cooperation. Special thanks also go to my colleague who helped during the project.

Apart from the technical support, I also would like to express my greatest gratitude to my advisor who has given me encouragement and guidance.

1.0 INTRODUCTION

1.1 BRAIN-COMPUTER INTERFACE AS AN ACCESS TECHNOLOGY

In everyday life, we use our vocal language, body language, gestures and facial expressions to enable communication with other people. However, individuals with severe physical disabilities are not able to live independent lives as they often lack alternative means of interacting with the surrounding world [1]. Therefore, finding effective and viable communication channels for them to overcome the communication barrier seems important and meaningful [2]. Hence, a variety of access technologies came into being and are being continuously researched and updated (e.g., [3]). Generally speaking, the idea of access technologies is to translate the intentions of users with physical disabilities into functional interactions such as communication and environmental control [2]. We have seen the use of mechanical devices to help people who suffer from physical impairments but still retain some ability of volitional body control. However, mechanical devices become less useful for patients who suffer from severe paralysis such as locked-in syndrome, a condition in which patients are completely paralyzed but fully aware [4]. For this population, we have to bring in new access technologies to enable their communication channels, and brain-computer interfaces (BCI) have demonstrated a great potential to break the silence [2].

The BCI, as an example of an access technology application, consists of two parts: access pathway and signal processing unit. An access pathway is defined as the actual sensors or input devices by which an expression of functional intent is transduced into an electrical signal [1]. By applying signal processing and pattern recognition techniques to these signals, we are able to build an interface as an electronic communication aid [5].

As mentioned above, a brain-computer interface (BCI) or brain-machine interface (BMI) allows the control of external devices using brain activities[2]. Direct communication between the outside world and patients who are suffering from locked-in syndrome can be achieved by processing available brain signals in real time through BCIs. Previously, functional imaging modalities employed for BCIs include electroencephalography (EEG), functional magnetic resonance imaging (fMRI) and near-infrared spectroscopy (NIRS) [6], [7]. EEG directly measures the neural activity, while fMRI and NIRS measure the blood hemoglobin concentration change associated with neural activity [8]. However, each of them has limitations that will be discussed later. Besides, nuclear imaging techniques such as photon emission computed tomography and positron emission tomography are also available; Nevertheless, researchers do not prefer these methods considering the measurements are difficult to replicate [9].

These noninvasive methods, unlike the invasive methods which inevitably carry risks associated with surgical implantation, will enjoy more acceptance, and that is why the imaging modalities have drawn so much attention. Therefore, exploring possibilities of building noninvasive but inexpensive BCIs is of great interest.

1.2 TRANSCRANIAL DOPPLER AS AN ACCESS PATHWAY

Various imaging techniques, such as functional magnetic resonance imaging, positron emission tomography, and single photon emission computed tomography, have been used to study brain functions [10], [11], [12]. In the past decades, the regional cerebral blood flow has been shown to be highly dependent on brain metabolism due to the need for O_2 and glucose [13]. Different from those typical imaging techniques, Transcranial Doppler (TCD), first introduced by Aaslid, Markwalder, and Nornes [14], allows for non-invasive investigation of cerebral blood flow with relatively high temporal resolution [13]. Researchers have taken advantage of the highly coupled relationship between the cerebral blood flow and brain activities to investigate human cognitive process [15]. Previous publications have successfully discussed the effect of gender (e.g., [16], [17]) and age (e.g., [18]) on the cerebral blood flow velocity using TCD. There are several major advantages of TCD. First, it is inexpensive to

acquire in comparison to other methods such as magnetic resonance imaging systems [12]. Second, TCD is relatively simple to operate meaning that experimental data acquisition or clinic diagnosis of neurological disorders such as stroke (e.g., [19]) is easily achievable. Therefore, TCD has been seen as a promising and powerful tool in monitoring of brain activities. Recently, functional TCD monitoring was proposed as an innovative way of building a brain-computer interface [20], [21], which increases our freedom to choose among access pathways (see Figure 1.1).

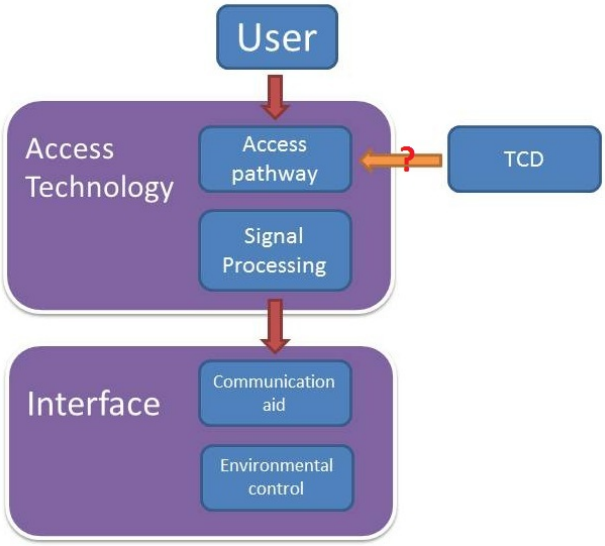

Figure 1.1: TCD as an access pathway.

1.3 TCD-BASED BRAIN-COMPUTER INTERFACE

TCD-based BCI, also a blood flow sensitive technique, is to some degree similar to fMRI and NIRS, which means they share the same drawbacks such as low spacial resolution. However, we are still interested in this technique because it is inexpensive, easy to set up and portable. Therefore we are trying to build a TCD-based BCI which can at least distinguish resting states and task states and send corresponding feedback. TCD itself has high temporal resolution in terms of the measurement of blood flow velocity, but it is possible that there exists some lag before detecting any observable CBFV increase when stimuli are applied, and we will consider this in our protocol design.

The traditional methods have shortcomings in multiple aspects. For example, the most commonly used method, EEG, is susceptible to electrical interference from environmental sources as well as artifacts such as electrooculography and electromyography [1]. Also, proficient use of EEG-based BCIs often involves several training sessions [20]. fMRI and MEG are too expensive and NIRS is premature. Given these limitations, we believe TCD is a new solution to brain computer interface.

1.4 COMPARISON OF DIFFERENT BRAIN-COMPUTER INTERFACE MODALITIES

As discussed, the focus of this research is on TCD. This section makes a brief comparison between TCD-based BCI and other types of BCI to demonstrate the feasibility of TCD.

Based on different methodological approaches, noninvasive BCI techniques exhibit different performances. However, the setup price range should also be taken into consideration. Assessing these modalities from a macro perspective, we regard TCD-based BCI as a promising imaging-based BCI candidate.

Compared with other BCI techniques, TCD-based BCI has decent temporal resolution (tens of milliseconds) but low spacial resolution because the perfusion can only be detected through large blood vessels [9]. Figure 1.2 is a summary of the resolution of different BCIs.

Generally, the invasive techniques have better resolution both spatially and temporally, but noninvasive techniques also have many comparative advantages. Table 1.1 compares different imaging-based BCI and lists their advantages and disadvantages.

1.5 RESEARCH OBJECTIVE

We are making our way towards building a brain-computer interface, and our current work seeks to solidify the foundation of the long term goal. In order to detect whether a cognitive activation exists, we need to find a baseline to be compared with, and hence we consider the resting state.

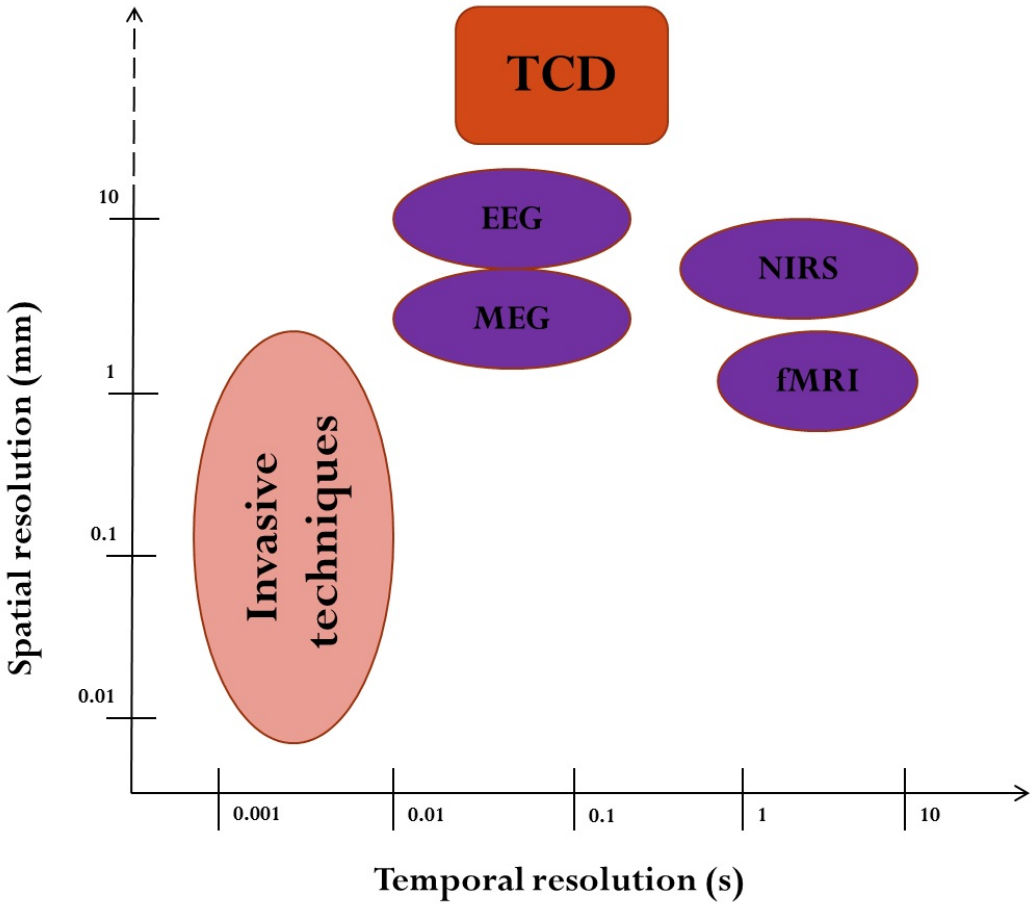

Figure 1.2: A schematic overview of the scale of spatial and temporal resolution of measurement methods used for BCI. Measurement methods are electroencephalography (EEG), magnetoencephalography (MEG), near-infrared spectroscopy (NIRS), functional magnetic resonance imaging (fMRI); adapted from Gerven [8].

The resting state describes brain activities without cognitive stimulus [22]. Therefore, the resting-state CBF information plays a key role in studying the CBF involving cognitive tasks. To properly characterize the resting-state cerebral blood flow, we are aiming to investigate features in multiple domains due to the complexity of human brain [23]. However, previous TCD studies only considered the so-called envelope signal (i.e., the peak values in the TCD

Table 1.1: Comparison of different imaging-based BCI; adapted from Min, Marzelli and Yoo [9].

Type	Cost	Advantages	Disadvantages
EEG	$\$5,000$	Good portability and affordability	Imperfection in spatial localization, marginal spatial resolution
		Excellent temporal resolution applicable for real-time BCIs	Involvement of inconvenient procedures during the placement of electrodes
		Good availability of paradigms and computational algorithms for BCI applications compared with other modalities owing to a relatively long developmental history	Difficulties in maintaining good electrodescalp contact and achieving long-term use of electrodes
MEG	$\$2-3$ million	Excellent temporal resolution applicable for real-time BCIs	Limited portability
		Superior spatial resolution and functional	High set-up and maintenance costs
			Requires dedicated electromagnetic shielding
fMRI	$>\$1$ million	Excellent spatial resolution	Limited temporal resolution associated with the inherent hemodynamic delay
		Data acquisition covering the entire brain volume	Limited portability
		Excellent source localization – advantageous for identification of function-specific loci	High set-up and maintenance costs
			Safety precaution required for ferromagnetic materials
			Requires dedicated electromagnetic shielding
NIRS	$>\$20,000$	Good portability and affordability	Limited temporal resolution associated with the inherent hemodynamic delay
		Metabolic specificity depending on infrared (IR) spectrum response	IR light occlusion by hair
		Uses corrosive-free sensors (e.g. optodes)	Optode size (requires spaces for both emitting and detecting IR light sources)
fTCD	$\$5,000$	Good portability	Difficulties in transcranial delivery of the ultrasound
		Ability to characterize the state of brain perfusion	Difficulties in adjustment of insonation path/focus
		Potential to actively modulate spatially-localized neuronal activity as BCI	Currently constrained to targeting large vessels

spectrum) [24], [25], [26]. By considering only the envelope signals, valuable information about cerebral blood flow characteristics may be lost. It is expected that the raw data, used

in calculation of the envelope signals, contains more comprehensive information about the resting-state characteristics.

In this research, we wish to investigate the significance of studying both the raw and the envelope signals. Secondly, following the previous study of the middle cerebral artery resting-state characteristics [27], my thesis presents a comparative study of cerebral blood flow in the anterior cerebral arteries using both the envelope signal and the raw data. Thirdly, we wish to find out whether there exist any gender effect or handedness effect. By completing these research objectives, we will be able to better understand the resting-state characteristics.

The thesis is outlined as follows: Chapter 2 provides the background knowledge regarding TCD-based BCI. Chapter 3 describes the data collection procedure. Chapter 4 introduces the basics of the techniques that we used for feature extraction. The extracted features are presented in chapter 5 as the research results. Chapter 6 discusses these results and finally, chapter 7 summarizes our findings and suggests the possible direction of future work.

2.0 BACKGROUND

2.1 ANTERIOR CEREBRAL ARTERY

There are three major cerebral arteries: middle cerebral artery (MCA), anterior cerebral artery (ACA) and posterior cerebral artery (PCA) [12]. In many publications assessing cognitive tasks using fTCD (e.g., [28], [29], [30]), the MCA is mostly insonated as over 80% blood delivery to the brain is achieved through MCA [12]. Also, cerebral blood flow through MCA is relatively easy to detect with the ultrasound probe due to the anatomical structure [31]. However, the ACA (60-75mm), which lies deeper than the MCA (35-60mm) [32], delivers blood to frontal lobes and superior medial parietal lobes [33]. As these regions are involved in receptive language and episodic memories [34], [35], [36], insonating ACA data appears to be viable as a complemental method to using solely MCA in understanding the resting-state characteristics of cerebral blood flow.

Figure 2.1 shows the approximate positions of the main cerebral artery anatomy and where the TCD probe can be placed to insonate these arteries.

2.2 MODELING THE CEREBRAL BLOOD FLOW

X In our study, the CBF velocity was measured using TCD based on an idealized CBF model shown in Figure 2.2. The velocity depends on the radius and reaches the maximum at the center or $r = 0$. The mathematical expression is [13]:

$$v(r) = K(R_0^2 - r^2) \tag{2.1}$$

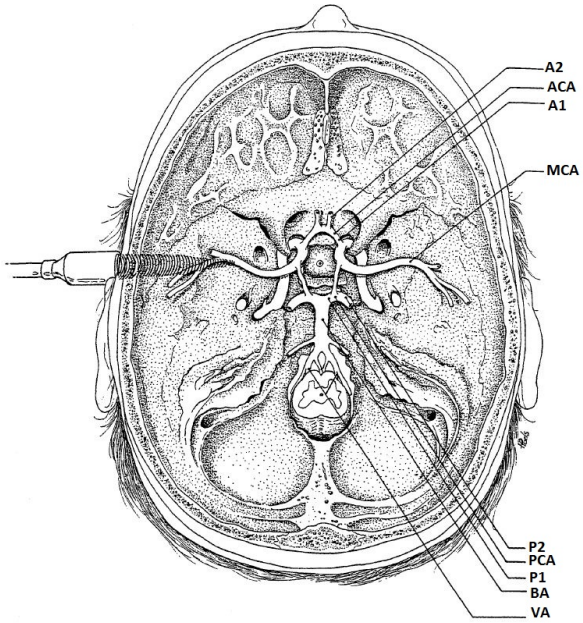

Figure 2.1: TCD insonation: The middle (MCA), anterior (ACA with A1 and A2), and posterior (PCA with P1 and P2) cerebral arteries, the basilar arteries (BA) and vertebral arteries (VA); adapted from Stroobant and Vingerhoets [25].

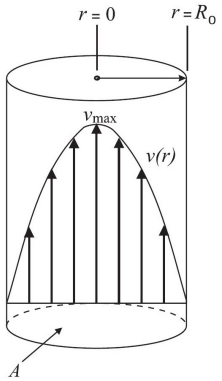

Figure 2.2: A model of idealized CBF; adapted from Deppe [13].

where K is assumed to be only a function of the pressure gradient and R_0 is the radius of the vessel. Therefore, if we define the mean velocity as [13]:

$$v_{mean} = \frac{1}{A}\int_A v(r)dA \tag{2.2}$$

where A is the cross-section area which equals πR_0^2, we can easily show that $v_{max} = 2v_{mean}$, and this v_{max} is usually called an envelope signal that is a part of this study [13], [12]. Figure 2.3 shows a blood vessel being insonated by a transducer. The blood vessel is modeled as a cylinder. We assume that: 1) the diameter does not change; 2) the insonnation angle θ describes the angle between the axes of the cylinder and the transducer.

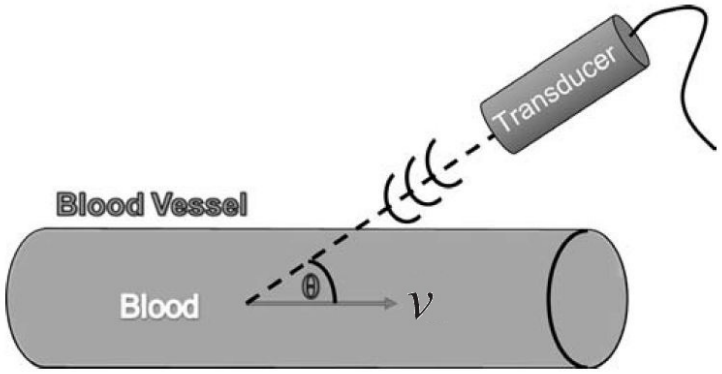

Figure 2.3: A blood vessel modeled as a cylinder; adapted from Azhari [37].

2.3 TRANSCRANIAL DOPPLER SONOGRAPHY

The cerebral blood flow velocity (CBFV) can be measured using transducers that produce and receive ultrasound. Based on Doppler effect, the spectral analysis provides an algorithm to calculate the CBFV.

2.3.1 Doppler effect

The Doppler effect is a physical phenomenon that describes the increase or decrease in frequencies when the propagating waves are reflected by moving objects. The typical example from daily life is that when a vehicle passes us by, the pitch of the blowing horn increases; when it travels away, the pitch goes down. People take advantage of this phenomenon to measure the blood flow velocity. Figure 2.4 shows a schematic diagram of the principle. An

object (erythrocyte) is moving in one direction in the vessel. The probe emits a sine wave towards the object and then receives the reflected wave for frequency analysis.

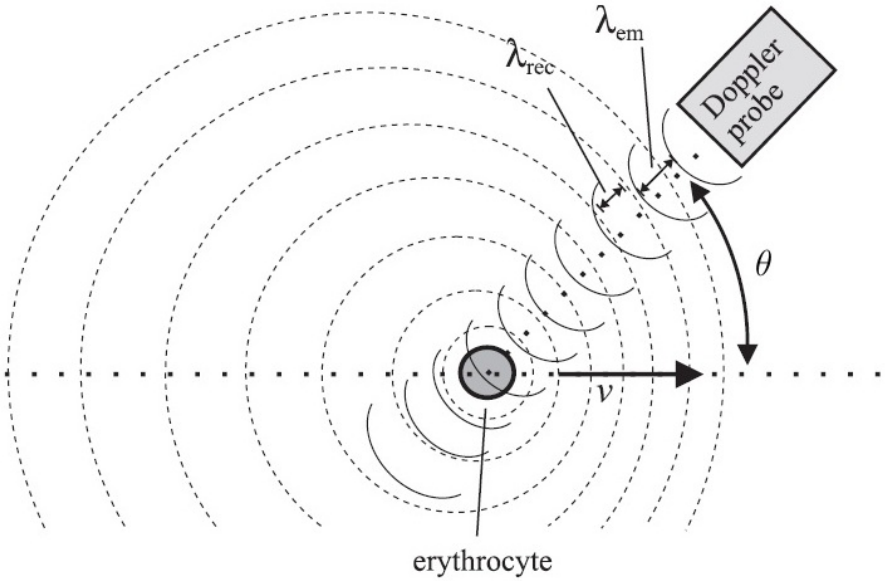

Figure 2.4: Insonation of a blood vessel at an angle θ; adapted from Deppe [13].

The relationship between the velocity and the frequency shift is quantified by the following relationship [37]:

$$v = \frac{c\Delta f}{2cos\theta f_0} \tag{2.3}$$

where f_0 denotes the frequency of the emitted pulsed signal, c denotes the ultrasonic traveling speed ($\approx 1500\, m/s$ in brain tissue) and θ is the insonation angle. By measuring the frequency shift, we will be able to estimate the velocity of the moving blood cells.

2.3.2 Doppler frequency shift estimation

One clinical requirement for the measurement is the information of the spacial location of the insonated vessel. Therefore, the transducer generates and sends pulse wave signals instead of continuous sinusoids. The depth can thus be calculated by measuring the time elapsed between sending one pulse and receiving its echo. On the other hand, the pulses are sent at a frequency that also represents the sampling frequency of the measurement. Therefore, it is

important to make the pulse repetition frequency larger than twice the maximum frequency of the desired signal. In this case, the frequency of the signal we consider corresponds to the Doppler frequency shift.

There are two ways of generating this signal. The first way is called quadrature demodulation that is achieved by mixing two signals and passing through low-pass filters. In this way, the received signal was sent into two channels simultaneously. The first one is multiplied by a cosine function at frequency f_0, and the other one is multiplied by a negative sine function at frequency f_0. The two obtained signals then pass through two low-pass filters respectively. Finally, they are considered as the real part and the imaginary part of the desired Doppler signal $Q(t)$ from received signal $s(t)$ (see Figure 2.5).

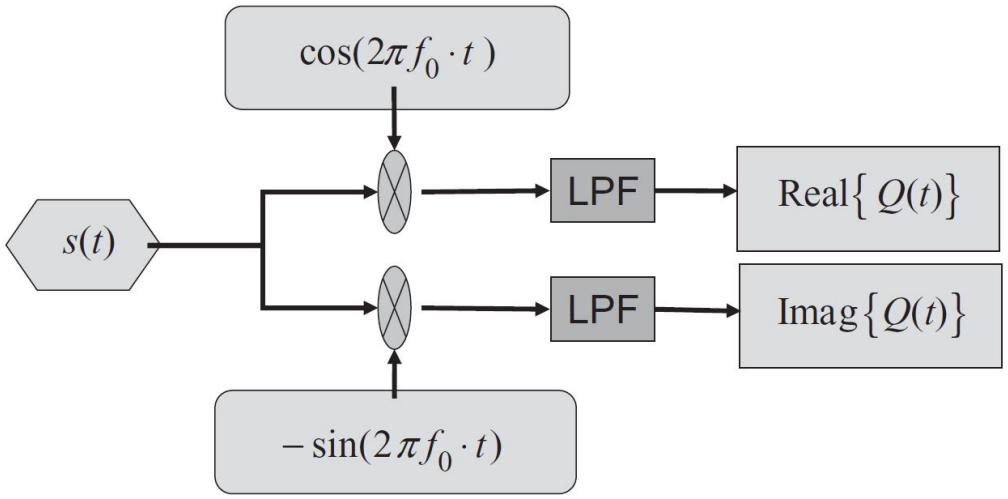

Figure 2.5: Composing $Q(t)$ using quadrature demodulation; adapted from Azhari [37].

Since $s(t)$ is a windowed cosine function, it can be described as $w(t)cos(2\pi ft)$ where $w(t)$ is a window function. Therefore, absent the low-pass filter:

$$s'(t) = w(t)cos(2\pi ft)[cos(2\pi f_0 \cdot t) - jsin(2\pi f_0 \cdot t)] \tag{2.4}$$

Using the Euler's formula, we obtain:

$$s'(t) = w(t)[e^{j\cdot 2\pi t(f-f_0)} + e^{-j\cdot 2\pi t(f+f_0)}] \tag{2.5}$$

We can see that equation 2.5 represents two frequency components in the square brackets. Since $f \approx f_0$, by adding a low-pass filter, we end up keeping the first term at frequency $(f - f_0)$ which is exactly the Doppler shift.

The second way involves the Hilbert transformation which is defined as [38]:

$$H\{S(t)\} = \frac{1}{\pi} \int_{-\infty}^{+\infty} \frac{S(t)}{(t-\tau)} d\tau \tag{2.6}$$

This transformation rotates the phase of the signal by 90 or -90 degrees depending on the

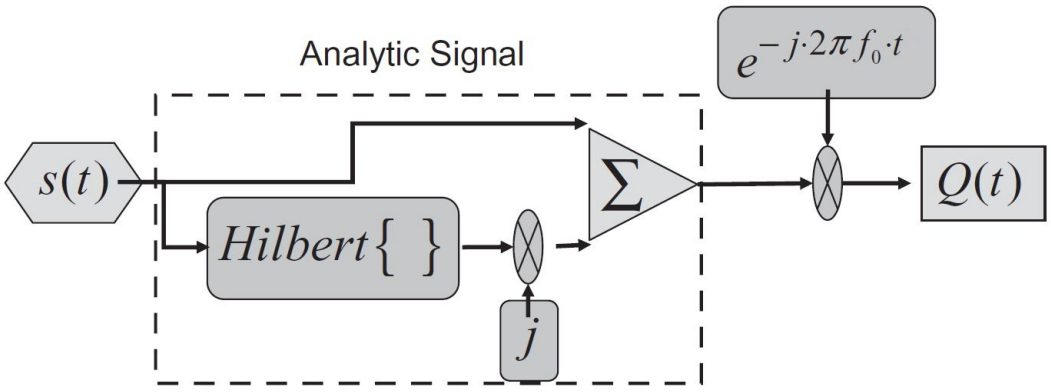

Figure 2.6: Composing $Q(t)$ using the Hilbert transformation; adapted from Azhari [37].

sign. Using Equation 2.6 and following structure shown in Figure 2.6, we will be able to construct the desired Doppler signal $Q(t)$ [37]. Using either method, we can find $Q(t)$ whose frequency component is the Doppler frequency shift that we are looking for.

$$Q(t) = w(t)e^{j\cdot 2\pi t(f-f_0)} \tag{2.7}$$

2.3.3 Velocity measurement

By plugging Equation 2.3 into Equation 2.7, we obtain the mathematical expression for $Q(t)$ in terms of the velocity v:

$$Q(t) = w(t)e^{j\cdot 2\pi t\left(cos\theta f_0 \frac{2v}{c}\right)} \tag{2.8}$$

In Figure 2.4, only one particle was shown for demonstration. However, when insonating the cerebral artery, we will detect many reflections by a large number of particles. Therefore, the detected signal consists of multiple frequencies and can be expressed as [13], [37],:

$$Q(t) = \sum_i a_i \cdot q_i(f_i, t) \tag{2.9}$$

where a_i is the amplitude of a sinusoidal function q_i. q_i represents the sinusoidal signals reflected by different moving particles. Therefore, each q_i contains a different frequency component.

We noticed that Equation 2.9 is in the form of Fourier series, and the Fourier transform will return the frequency components, i.e. the velocity of the blood cells. A TCD device calculates the a_i by Fast Fourier Transform (FFT) within a time period, selects the maximum value, and then displays the results in a spectrum.

2.3.4 Using relative velocity

For one single pulse, we collected many frequencies, i.e. velocities, reflected by particles in the blood vessel. Therefore, the intensity-weighted mean velocity which is defined as the CBFV in 2.2 can be approximated using the mean frequency shift. The mean frequency shift $\Delta f = f - f_0$ is defined as [39]:

$$\Delta f_{mean} = \frac{\sum_i a_i \Delta f_i}{\sum_i a_i} \tag{2.10}$$

This definition provides us a way to evaluate the overall frequency shifts due to the superposition of different blood cells.

2.3.5 Raw signal and envelope signal

In our study, the raw signal $Q(t)$ given in equation 2.7 was exported and considered. Figure 2.7 gives an example of the raw signal. As a comparison, figure 2.8 gives an example of the corresponding four periods of the envelope signal.

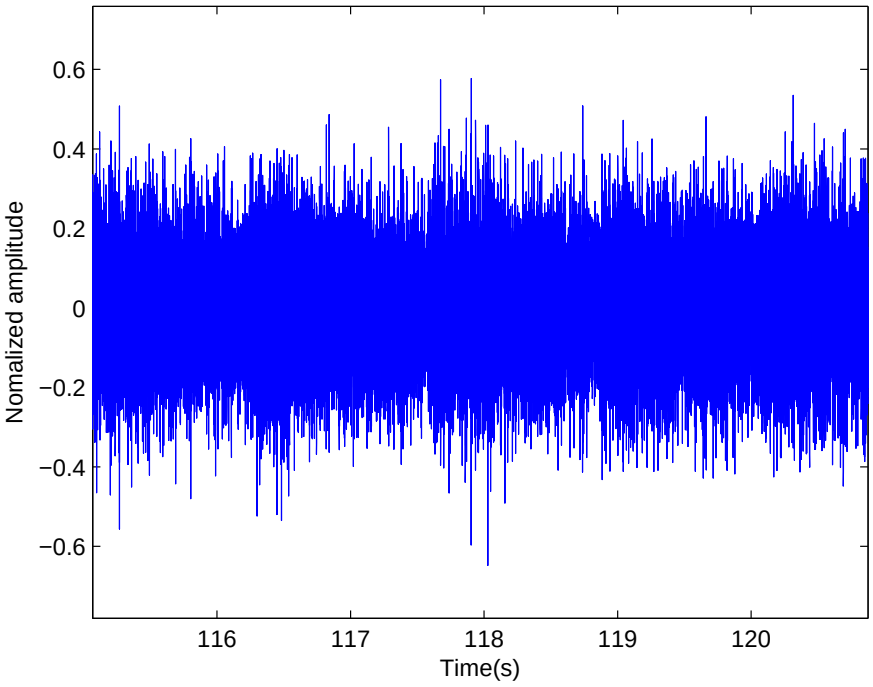

Figure 2.7: An example of $Q(t)$ exported from participant's R-TCD channel.

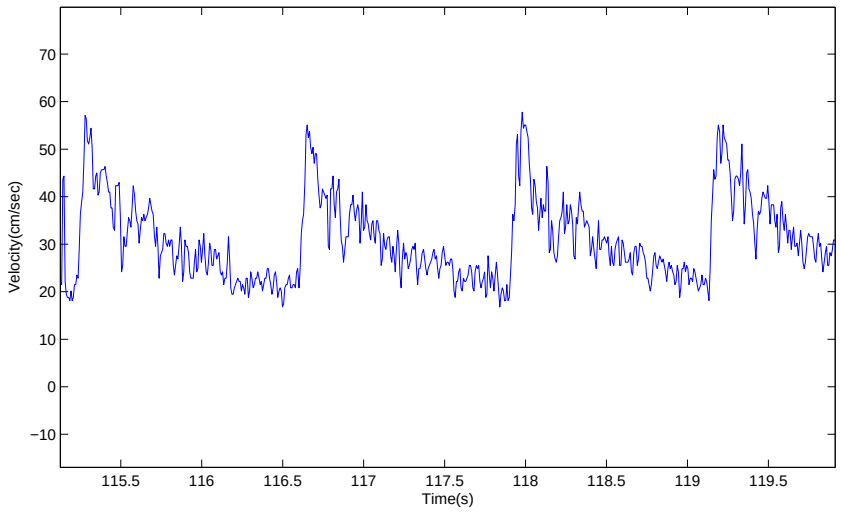

Figure 2.8: An example of an envelope signal calculated based on $Q(t)$.

3.0 PROTOCOL DESIGN AND DATA ACQUISITION

This chapter includes two aspects of the protocol design. The goal is to collect data to obtain sufficient information to characterize resting-state ACA blood flow.

3.1 SUBJECTS

The cerebral blood flow velocity data was collected from 20 healthy voluntary subjects, 9 males and 11 females. The subjects were first requested to read through and sign the consent form that has been approved by the University of Pittsburgh Institutional Review Board. None of the participants had a history of heart murmurs, strokes, concussions, migraines or any other brain or neurological conditions. Basic anthropometric information including age, height, and weight was also collected. Table 3.1 summarizes the demographic information of the consenting participants.

Table 3.1: Participants' demographic information.

Distribution	Male	Female	Overall
Age	22.3 ± 1.64 years old	22.0 ± 2.00 years old	22.1 ± 1.86 years old
Height	180 ± 7.26 cm	163 ± 5.39 cm	171 ± 10.1 cm
Weight	91.6 ± 29.3 kg	52.6 ± 5.89 kg	68.9 ± 27.3 kg

The handedness of each participant was assessed using the Edinburgh Handedness Inventory [40] before data acquisition, and the result was scored based on the formula below:

$$\text{Handedness Score} = \frac{\sum_{i=1}^{N} X(i,R) - \sum_{i=1}^{N} X(i,L)}{\sum_{i=1}^{N} X(i,R) + \sum_{i=1}^{N} X(i,L)} \tag{3.1}$$

where $X(i, L/R)$ is evaluated as either 1 (preferred) or 2 (dominant) for the left (right) hand doing certain activities. The subjects' scores are summarized in Table 3.2.

Table 3.2: Participants' handedness distribution.

	Right-handed	Left-handed	Bidextrous
Number of subjects	16	3	1
Gender	8 males	2 females	1 female
Average score	64	-63	0

3.2 PROCEDURE

Bilateral cerebral blood flow in the ACA was measured using a SONARA TCD system (CareFusion, San Diego, CA, USA) with two 2 MHz transducers placed on the transtemporal window through which the ultrasound can penetrate the skull and reach the arteries [12]. Since the ACA and the MCA are anatomically close to each other [31], the signal was obtained by slightly rotating the probes after the MCA signal was obtained (see Figure 3.4 and 3.5). This adjustment could be nontrivial, but the blood flow from two arteries is easily distinguishable. The direction of the blood flow in the ACA is opposite to the blood flow in the MCA [24]. The depth of the ACA is about 10-15mm deeper than the MCA, which also serves as an indicator that the ACA has been successfully insonated. The TCD system interface displays a time-frequency representation of the envelope signal (see figure 3.2). The intensity of the detected velocity were represented according to the color bar.

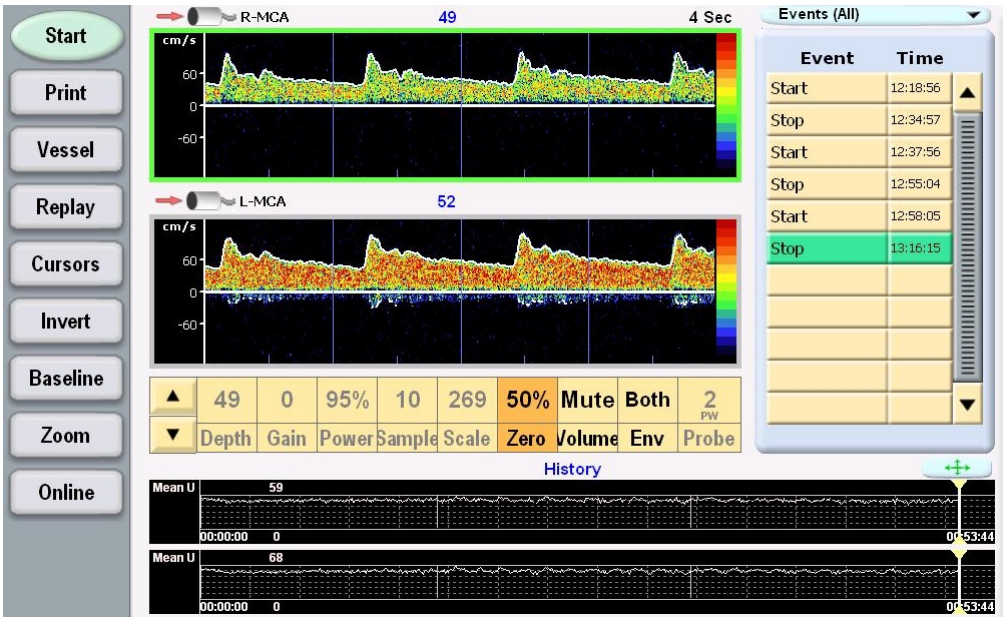

Figure 3.1: An example of a MCA measurement display on TCD. The MCA is usually detected before the ACA.

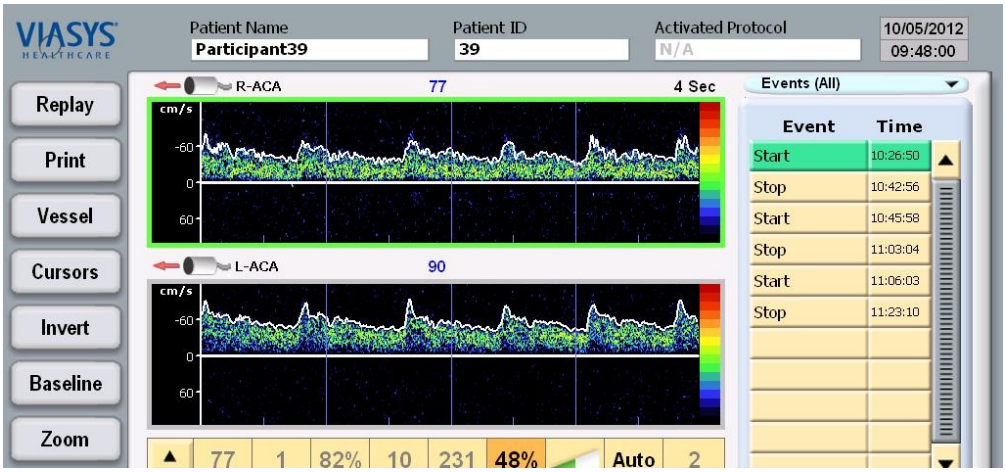

Figure 3.2: An example of a ACA measurement display on TCD.

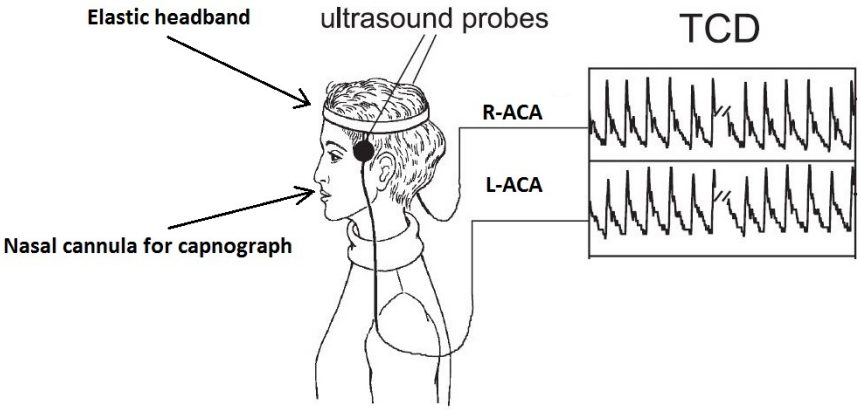

Figure 3.3: A bilateral insonation setup; adapted from Deppe [13].

The data acquisition (see Figure 3.3) lasted for 15 minutes for each participant. The participants were requested to keep quiet and as thought-free as possible during this process. The probes were fixed using an elastic headband to around 5 cm in front of the ears, above the zygomatic arch [41] (see Figure 3.4). The specific insonation location may vary depending

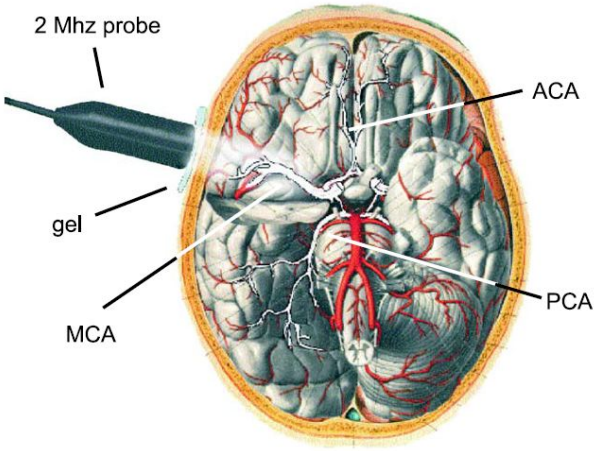

Figure 3.4: MCA insonation; adapted from Deppe [13].

on the signal intensity obtained by the TCD system from different subjects. The end-tidal carbon dioxide was monitored throughout the data acquisition using the BCI Capnocheck

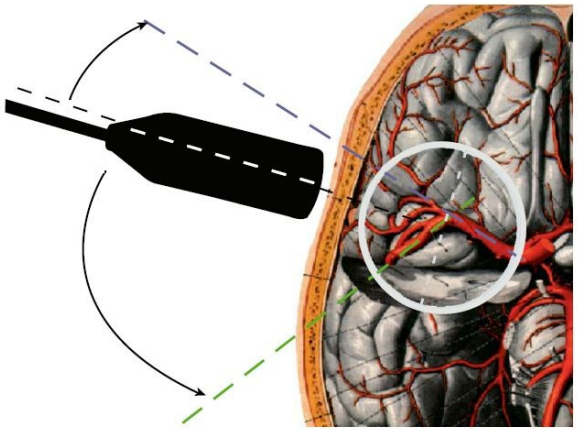

Figure 3.5: Gently rotate the probe when the MCA is detected to obtain the ACA; adapted from Deppe [13].

Sleep (Smiths Medical PM, Inc. Waukesha, Wisconsin, USA). The subjects were also fitted with sensors to record the electrocardiogram, respiration rate, skin conductance and head movement during the recordings. These sensors are part of a multisystem physiological data monitoring system made by Nexus-X (Mindmedia, Netherlands). Participants also completed some additional tasks afterwards, which is not part of the current study.The raw data was extracted as audio files with a sampling frequency of 44100 Hz. They were downsampled by a factor of 5 to speed up the computation since the TCD system uses a low-pass filter which filters out the frequency components above the maximum scale value that we configured in advance.

4.0 FEATURE EXTRACTION

To carry out the comparative analysis, we considered a range of features using classical and modern analysis tools.

4.1 STATISTICAL FEATURE

Three basic parameters widely used in statistics: standard deviation, skewness and kurtosis [38], were employed to characterize (e.g., [42], [43]) the ACA signal from the left channel (L-ACA) and the right channel (R-ACA), respectively. The cross-correlation between the L-ACA and R-ACA is also considered. The zero-lag value was calculated by selecting the maximum coefficient in the obtained sequences.

Assume we have two signals x and y. The definitions mentioned above are mathematically expressed and listed below. A typical way to compute the standard deviation is:

$$\sigma_X = \sqrt{\frac{1}{n-1}\sum_{i=1}^{n}(x_i - \mu_X)^2} \tag{4.1}$$

where μ_X denotes the mean value. The skewness is defined as:

$$\epsilon_X = \frac{\frac{1}{n}\sum_{i=1}^{n}(x_i - \mu_X)^3}{[\frac{1}{n}\sum_{i=1}^{n}(x_i - \mu_X)^2]^{3/2}} \tag{4.2}$$

The kurtosis of the distribution is computed as:

$$\gamma = \frac{\frac{1}{n}\sum_{i=1}^{n}(x_i - \mu_X)^4}{\left(\frac{1}{n}\sum_{i=1}^{n}(x_i - \mu_X)^2\right)^2} \tag{4.3}$$

The zero-lag cross-correlation coefficient is defined as:

$$CC_{XY} = \sum_{i=1}^{n} x_i y_i \tag{4.4}$$

4.2 INFORMATION-THEORETIC FEATURE

4.2.1 Lempel-Ziv complexity

The information-theoretic features have been extensively utilized in the analysis of neurological analysis (e.g., [44], [45]). The Lempel-Ziv complexity [46], the conditional entropy [45] and the cross-conditional entropy [45] have been used to measure the complexity and regularity of biomedical signals. They provide us with indices reflecting the signals from predictability and randomness point of views.

To calculate the Lempel-Ziv complexity, we first quantized the objective signal into 100 levels, so the signal X_n can be expressed as $[x_1, x_2 \ ... \ x_n]$ in terms of the quantized levels. Then these points were grouped in blocks of a length of L, where L increases from 1 to n. Let $P_s(i, j)$ denote the block $[x_i, x_{i+1}, \ ... \ x_j]$ for all $i < j$. Then for each L, we check if P_s has already appeared with previous i and j. If not, we put this block as one element into a set, V. Finally, let $c(n)$ denote the number of elements in the set V, i.e., the number of distinct parsed blocks P_s, and the LZC is then defined as follows:

$$LZC = \frac{c(n)(\log_{100} c(n) + 1)}{n} \tag{4.5}$$

4.2.2 Conditional entropy

To calculate the conditional entropy (CE), the process x_i is normalized and grouped in blocks of length L, $10 \leq L \leq 30$, such that $S_L(i) = [x(i), x(i-1), ...x(i-L+1)]$. CE is then calculated (see 4.6) using the joint probability of the previous $L-1$ samples and their values (i.e., X_{L-1}) [45]. Due to the underestimation of CE for larger L, [45] a corrective term, $perc(L)SE(1)$ (see 4.7) was added to CE, where $SE(1)$ is the Shannon entropy [47], and $perc(L)$ is the percentage of length L blocks found only once in the process.

$$CE(L) = -\sum_{L-1} p(x_{L-1}) \sum_{i|(L-1)} p(x(i)|x_{L-1}) \ln p(x(i)|x_{L-1}) \tag{4.6}$$

where $p(x_{L-1})$ is the joint probability of the pattern x_{L-1} and $p(x(i)|x_{L-1})$ is the conditional probability of $x(i)$ given x_{L-1}.

$$SE(1) = -\sum_{L} p(x(i)) \ln p(x(i)) \tag{4.7}$$

Then, the regularity index is defined as:

$$\rho = 1 - min \left\{ \frac{CE(L) + prec(L)SE(1)}{SE(1)} \right\} \tag{4.8}$$

Synchronization index (χ_{xy}) can be measured by extending and modifying the regularity index formula [45]. Instead of making use of the previous $L-1$ samples in the self signal, x_{L-1}, we replace it with those of the synchronized signal, y_{L-1}. The joint probability thus involves the current $x(i)$ being looked at and the previous $L-1$ samples in y. The synchronization index is then defined as

$$\chi_{xy} = 1 - min \left\{ \frac{CExy(L) + prec(L)SEy(1)}{SEy(1)}, \frac{CEyx(L) + prec(L)SEx(1)}{SEx(1)} \right\} \tag{4.9}$$

where $CE_{xy}(L)$ is the conditional entropy of the current x given the previous $L-1$ y sample points, and similarly, $CE_{yx}(L)$ denotes the conditional entropy of the current y given the previous $L-1$ x sample points.

4.3 FREQUENCY ANALYSIS

4.3.1 Basics of Frequency analysis

The frequency analysis is based on the investigation of the frequency components of a signal – a function in terms of the time, t. The Fourier transform is a mathematical transform that converts a function with argument t into a function with argument f, the frequency, and various characteristics can be then studied in the frequency domain. However, in order to implement computation of the original definition of the Fourier transform which involves integrals, we digitalize the signal in both time domain and frequency domain, where we need to employ sampling theory and make use of the discrete Fourier transform which is defined as equation 4.10:

$$X_k = \sum_{n=0}^{N-1} x_n \cdot e^{-j \cdot 2\pi k n / N} \tag{4.10}$$

where x_n is a time series indexed by n (a discrete-time signal), and N is the length of this signal. To do this transform, we have assumed the periodicity of the signal in time domain. This causes a problem when downsampling is applied because aliasing might happen. Therefore, in the next section in this chapter where downsapling is mentioned, we guarantee that the filters have some low-pass characteristics so that aliasing can be avoided.

4.3.2 Frequency features

In the frequency domain, the following parameters were utilized:

The peak frequency (f_p) is defined as the frequency which has the largest squared value in the frequency spectrum [48]:

$$f_p = \text{argmax}_f \left\{ |F_X(f)|^2 \right\} \tag{4.11}$$

It measures the frequency value where the largest power occurs.

The centroid frequency (f_c) measures the center of frequency components in the spectrum taking center of mass as an analogy [49]. It is defined as:

$$f_c = \frac{\int_0^{f_{max}} f|F_X(f)|^2 df}{\int_0^{f_{max}} |F_X(f)|^2 df} \tag{4.12}$$

The bandwidth (BW) of the spectrum is a measure of the spreadness of the frequency components [50]. It is defined as:

$$BW = \sqrt{\frac{\int_0^{f_{max}} (f - f_c)^2 |F_X(f)|^2 df}{\int_0^{f_{max}} |F_X(f)|^2 df}} \tag{4.13}$$

where F_X in (4.12) and (4.13) is the Fourier transform of the original signal.

4.4 TIME-FREQUENCY ANALYSIS

4.4.1 The scaling function

In order to express a function using two parameters, we need to define the scaling function. Taking Fourier series as an analogy, a function $f(t)$ can be written as a linear combination of some base functions, which means [51]:

$$f(t) = \sum_k A_k \varphi_k(t) \tag{4.14}$$

where $\varphi_k(t)$ is the scaling function defined as [51]:

$$\varphi_k = \varphi(t - k) \tag{4.15}$$

and A_k is a coefficient associated with the term φ_k. In order to make a time-frequency expression, we add another parameter j such that we have not only the ability to shift the scaling function in time, but also the freedom to expand and shrink the function around the origin [51]. Therefore the two-dimensional scaling function is defined as:

$$\varphi_{j,k}(t) = 2^{j/2} \varphi(2^j t - k) \tag{4.16}$$

4.4.2 The Discrete Wavelet Transform

This section covers the basics of discrete wavelet decomposition (DWT). Equation 4.16 shows that the scaling function φ can be expressed as a linear combination of shifted $\varphi(2t)$, therefore [51]:

$$\varphi(t) = \sum_k h(k)\sqrt{2}\varphi(2t-k) \tag{4.17}$$

where $h(k)$ is a sequence called the scaling function coefficients. $\sqrt{2}$ is there to maintain the norm of the scaling function.

However, it has been shown that a signal can be better described by defining another set of function $\psi(t)$ that spans the difference between the spaces spanned by two scaling functions [51]. Following the same idea, the mother wavelet is defined as:

$$\psi_{j,l}(t) = 2^{j/2}\psi(2^j t - l) \tag{4.18}$$

and a similar form to 4.17 can be obtained

$$\psi(t) = \sum_l h_1(l)\sqrt{2}\psi(2t-l) \tag{4.19}$$

The scaling function φ and mother wavelet ψ together form a wavelet [51]. We also require the scaling functions form a set of orthogonal basis on jth level. That is:

$$\int \varphi_{j,l}(t)\varphi_{j,k}(t)dt = 0 \tag{4.20}$$

Now, using 4.17 and 4.19, given a general function $g(t)$, we can write it into the expression as follows:

$$g(t) = \sum_k a_{j_0}(k)2^{j_0/2}\varphi(2^{j_0}t-k) + \sum_k \sum_{j=j_0}^{\infty} d_j(k)2^{j/2}\psi(2^j t-k) \tag{4.21}$$

where $2^{j/2}$ serves to maintain the norm just like the term $\sqrt{2}$ in 4.17 and 4.19. c_j and d_j are the coefficient sequences.

Because we are dealing with orthonormal basis, along with 4.17 and 4.19, using the inner product $a_j(k) = \langle g(t),\ \varphi_{j,k}(t)\rangle$, we can find that the coefficients satisfy:

$$a_j(k) = \sum_m h(m-2k)a_{j+1}(m) \tag{4.22}$$

$$d_j(k) = \sum_m h_1(m - 2k)a_{j+1}(m) \tag{4.23}$$

Equations 4.22 and 4.23 are in the form of convolution and we can employ the idea of filtering in digital domain to complete the decomposition. The scale of 2 can be generated by downsampling. Therefore, an algorithm that generates the coefficients can be described as below(see Figure 4.1). The obtained d_i represents the coefficient of the mother wavelet on the ith level (detail coefficient). a_i is the coefficient of the scaling function (approximate coefficient). The filters h and h_1 can be designed based on equations 4.17 and 4.19

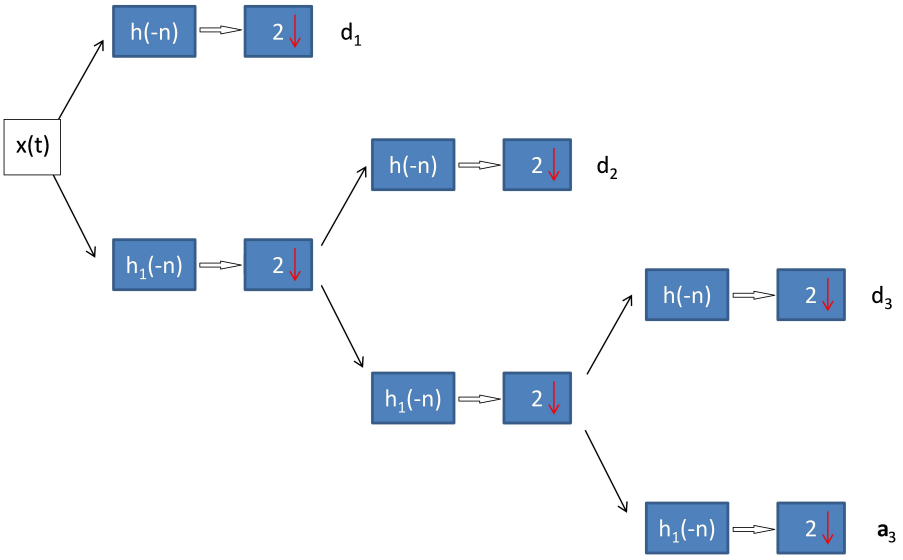

Figure 4.1: A 3-level discrete wavelet decomposition using filters.

4.4.3 Time-frequency features

The 10-level Meyer discrete wavelet decomposition was applied to the obtained signals and the relative energy and energy entropy were considered [52]. The scaling function and the mother wavelet are shown in Figure 4.2 According to Parseval's theorem, the energy on each level adds up to the total energy of the original signal (see equation 4.24). In time-frequency domain, this can be thought of as the partitioning of the time-scale plane.

$$\int |g(t)|^2 dt = \sum_{l=-\infty}^{\infty} |a(l)|^2 + \sum_{j=0}^{\infty} \sum_{k=-\infty}^{\infty} |d_j(k)|^2 \tag{4.24}$$

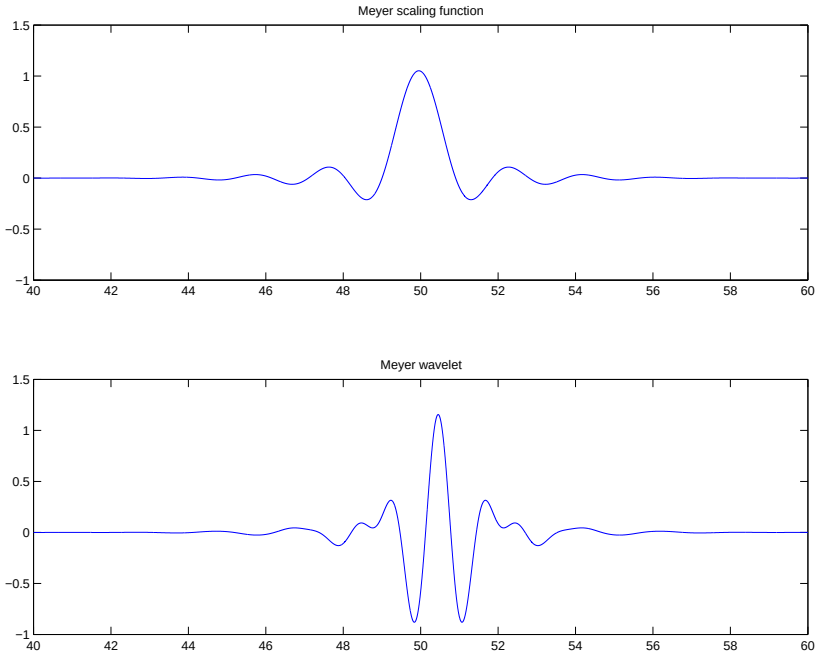

Figure 4.2: Meyer wavelet and its scaling function.

The relative energy is defined as the ratio between the energy at the ith level (E_i) and the total energy (E_{total}). E_{total} is calculated as the Euclidean norm [52], [53] of the vector $V = [a_{10}, d_{10}, d_9, ...d_1]$, where a_{10} denotes the approximation coefficient and d_i denotes the detail coefficient at the ith level [54]. The mathematical expressions are:

$$E_{total} = \|V\| \tag{4.25}$$

$$E_a = \frac{a^2}{E_{total}} \tag{4.26}$$

$$E_{d_i} = \frac{d_i^2}{E_{total}} \tag{4.27}$$

The wavelet entropy can be regarded as a measure of how well the process behaves, or in other words, a measure of information distribution [52].

$$WE = -\sum_{i} E \log_2 E \tag{4.28}$$

where E is the relative energy calculated above in (4.25). A lower value of WE (close to 0) implies that the wavelet energy is relatively concentrated on a certain band. On the contrary, a more random process would result in a higher value of WE which represents the spreadness of the wavelet energy over many decomposed levels.

4.5 WILCOXON RANK-SUM TEST

The Wilcoxon rank-sum test, a non-parametric statistical hypothesis test [55], was used to infer about statistical differences. One advantage is that when using this method, we do not have to assume that the distribution of the extracted features adheres to the Gaussian distribution. The null hypothesis in this test is that the medians are equal. The idea of using this test is to check whether the sample sets are from the same distribution.

Suppose we have two sets of data $X = [x_1, x_2, x_3, ..., x_n]$ and $Y = [y_1, y_2, y_3, ..., y_m]$ which in our case would be the extracted features obtained from the right and left channel respectively. The length of the feature sets do not have to be the same in order to use the rank-sum test. But in our research, we dealt with the same length for the left and right signals because bilateral insonation were processing simultaneously and the sampling rate applied to both channels is the same. The first step is to combine X and Y to construct a new array, and sort all the elements in ascending order. We then label each element with the group it belongs to and its order number ranked in the newly constructed array. Figure 4.3 shows an example of assigning the rank numbers to elements. If adjacent elements happen to hold the same value, we assign the median to each of them.

$Data:$	n_1	n_2	n_3	n_4	n_5	n_6	n_7	n_8	n_9	...	n_{n+m}
$From:$	X	Y	X	Y	Y	X	Y	X	Y	...	X
$Rank:$	1	2	3.5	3.5	5	6	8	8	8	...	$n+m$

Figure 4.3: Elements are sorted in ascending order and labeled with group and ranking.

In the example in Figure 4.3, we need to add up all ranks of X, $s_X = 1{+}3.5{+}8{+}....{+}n{+}m$, which is called the rank-sum of X. Considering that for different distributions of X and Y, the value of s_X varies from $\frac{(1+n)\cdot n}{2}$ to $\frac{(2n+m+1)\cdot m}{2}$, we assign a random variable S_X to it. Therefore, we can define the p value as:

$$p = \begin{cases} 2\mathrm{P}(S_X \geq s_X) & \text{if } s_X \text{ is in the upper tail} \\ 2\mathrm{P}(S_X \leq s_X) & \text{if } s_X \text{ is in the lower tail.} \end{cases} \tag{4.29}$$

The exact p value can be calculated by counting the number of all combination that satisfy 4.29.

5.0 RESULTS

To safely present the TCD measurement results, we firstly exclude the possibility that the features were influenced by the end-tidal carbon dioxide level [56]. Firstly, by taking linear regression test, no evidence was found that the $ETCO_2$ level was affected by the Body Mass Index (BMI) for either gender (shown in Table 5.1). Secondly, we observed the trend of the CO_2 recording for every participant and found no dramatic fluctuation exists.

Table 5.1: $ETCO_2$ level and BMI.

	BMI (m/kg^2)	CO2 (mmHg)	p-value
Male	28.1 ± 8.30	32.0 ± 3.86	0.94
Female	19.7 ± 1.66	35.4 ± 2.70	0.32

5.1 STATISTICAL FEATURE

A summary of statistical feature values for the envelope signals (mean ± standard deviation) is presented in Table 5.2. A high cross-correlation between the left and right ACA blood flow was obtained for all subjects. The standard deviation, which represents how far the sample data deviate from the mean, was found to be statistically higher in the female group than in the male group (R-ACA: $p = 0.04$; L-ACA: $p = 0.01$). The female group also has statistically higher skewness (R-ACA: $p = 0.04$; L-ACA $p = 0.03$) and kurtosis than the male group ($p < 0.05$ for both channels). When comparing the left-handed group with the right-

Table 5.2: Statistical features for the envelope signals.

	Male	Female	Left-handed	Right-handed
$StddeviationR$	11.4 ± 2.48	16.0 ± 4.18	17.7 ± 4.64	13.3 ± 3.75
$StddeviationL$	11.1 ± 3.06	18.2 ± 6.19	17.7 ± 4.61	14.6 ± 6.28
$SkewnessR$	1.73 ± 1.04	0.90 ± 0.64	0.96 ± 0.09	1.33 ± 1.01
$SkewnessL$	1.33 ± 0.49	0.85 ± 0.46	1.07 ± 0.42	1.06 ± 0.55
$KurtosisR$	8.81 ± 7.57	4.54 ± 2.44	3.87 ± 0.61	6.92 ± 6.17
$KurtosisL$	6.31 ± 2.84	3.98 ± 1.47	4.19 ± 1.37	5.18 ± 2.60
$Crosscorrelation$	0.93 ± 0.04	0.90 ± 0.05	0.88 ± 0.05	0.92 ± 0.88

handed group, however, fairly high p-values for both channels (skewness: $p > 0.40$; kurtosis: $p > 0.68$) were obtained. That implies that the null hypothesis could not be rejected.

Table 5.3: Statistical features for the raw signals. * denotes multiplication by 10^{-3}.

	Male	Female	Left-handed	Right-handed
$StddeviationR$	0.15 ± 0.04	0.10 ± 0.02	0.09 ± 0.02	0.13 ± 0.04
$StddeviationL$	0.14 ± 0.01	0.09 ± 0.02	0.09 ± 0.01	0.12 ± 0.05
$SkewnessR$	$(-0.50 \pm 5.42)^*$	$(-1.94 \pm 8.84)^*$	$(-0.19 \pm 2.71)^*$	$(0.12 \pm 5.08)^*$
$SkewnessL$	$(-0.10 \pm 2.54)^*$	$(2.06 \pm 8.70)^*$	$(7.08 \pm 10.1)^*$	$(-0.76 \pm 4.41)^*$
$KurtosisR$	3.49 ± 0.49	3.87 ± 1.65	3.45 ± 0.56	3.46 ± 0.74
$KurtosisL$	3.33 ± 0.33	4.41 ± 3.18	3.69 ± 0.92	3.32 ± 0.31
$Crosscorrelation$	0.01 ± 0.01	$(3.18 \pm 1.67)^*$	$(2.80 \pm 1.27)^*$	$(5.12 \pm 8.65)^*$

Similarly, the statistical feature for the raw signals are presented in Table 5.3. Unlike the results for the envelope signals, statistical difference between males and females was only found in the standard deviation values (R-ACA: $p < 0.01$; L-ACA: $p = 0.01$). Another major discrepancy is that the cross-correlation between the left channel and the right channel is

relatively lower in the raw signal (≈ 0.01), which represents that the dependence in the raw signals is lower than that in the envelope signals.

5.2 INFORMATION-THEORETIC FEATURE

Table 5.4: A summary of information-theoretic features for the envelope signals. * denotes multiplication by 10^{-3}.

	Male	Female	Right-handed	Left-handed
$LZCR$	0.65 ± 0.04	0.68 ± 0.04	0.66 ± 0.04	0.70 ± 0.01
$LZCL$	0.67 ± 0.03	0.70 ± 0.03	0.70 ± 0.04	0.69 ± 0.01
$RegularityindexR$	0.08 ± 0.07	0.04 ± 0.05	0.07 ± 0.06	$(9.63 \pm 4.58)^*$
$RegularityindexL$	0.04 ± 0.04	0.03 ± 0.04	0.04 ± 0.04	0.02 ± 0.01
$Synchronization$	0.15 ± 0.07	0.13 ± 0.08	0.15 ± 0.08	0.09 ± 0.04

Table 5.5: A summary of information-theoretic features for the raw signals.

	Male	Female	Right-handed	Left-handed
$LZCR$	0.68 ± 0.03	0.70 ± 0.03	0.69 ± 0.03	0.70 ± 0.02
$LZCL$	0.68 ± 0.03	0.68 ± 0.05	0.69 ± 0.03	0.68 ± 0.05
$RegularityIndexR$	0.38 ± 0.17	0.25 ± 0.15	0.30 ± 0.16	0.22 ± 0.14
$RegularityindexL$	0.37 ± 0.15	0.31 ± 0.25	0.31 ± 0.18	0.34 ± 0.27
$Synchronization$	0.37 ± 0.17	0.27 ± 0.19	0.30 ± 0.17	0.27 ± 0.15

The information-theoretic features of the envelope signal are presented in Table 5.4. The calculations of Lempel-Ziv complexity do not show any statistical difference on either channel between females and males ($p > 0.08$), nor between left-handed and right-handed ($p > 0.09$). The regularity index on both channels is low, but the synchronization is relatively higher.

This implies that the signal is more predictable by looking at the opposite channel than looking at itself.

Table 5.5 shows the feature values of the raw signals. The mean values of Lempel-Ziv complexity (≈ 0.68) are similar to those calculated for the envelope signals. However, the raw signals have higher regularity than the envelope signal in the time domain ($p < 0.01$). The raw signals also have higher synchronization than the envelope signal ($p < 0.01$), which means the raw signals from the two channels contain more mutual information. In terms of the value of the regularity and synchronization index, neither gender-based ($p > 0.17$) nor handedness-based ($p > 0.13$) statistical difference was found.

5.3 FREQUENCY DOMAIN FEATURE

Table 5.6 summaries the features in the frequency domain of the envelope signals, and Table 5.7 summaries the features of the raw signals. The envelope signals have low frequencies around 11–14 Hz. The peak frequencies appeared to be person-specific since the standard deviation is high compared to its mean. No statistical difference between males and females or between right-handed and left-handed subjects could be concluded for any of these feature values ($p > 0.05$).

Table 5.6: Frequency domain features for the envelope signals. * denotes multiplication by 10^{-3}.

	Male	Female	Right-handed	Left-handed
$CentroidfrequencyR$	11.9 ± 4.79	14.9 ± 4.02	12.9 ± 4.49	17.5 ± 3.34
$CentroidfrequencyL$	11.7 ± 3.74	15.6 ± 3.89	13.7 ± 4.14	14.4 ± 5.07
$PeakfrequencyR$	0.69 ± 0.51	0.42 ± 0.55	0.64 ± 0.55	$(4.41 \pm 5.42)^*$
$PeakfrequencyL$	0.57 ± 0.50	0.32 ± 0.52	0.51 ± 0.54	$(2.97 \pm 3.02)^*$
$BandwidthR$	12.6 ± 2.52	13.9 ± 1.00	13.2 ± 2.08	14.2 ± 0.16
$BandwidthL$	12.9 ± 1.54	13.9 ± 1.09	13.5 ± 1.38	13.5 ± 1.53

Table 5.7: A summary of frequency domain features for the raw signals.

	Male	Female	Right-handed	Left-handed
$CentroidfrequencyR$	855 ± 198	1090 ± 197	979 ± 239	1060 ± 183
$CentroidfrequencyL$	850 ± 201	1060 ± 207	961 ± 232	1050 ± 209
$PeakfrequencyR$	523 ± 206	631 ± 259	603 ± 212	642 ± 241
$PeakfrequencyL$	526 ± 168	723 ± 543	526 ± 162	628 ± 107
$BandwidthR$	627 ± 90.4	743 ± 81.5	682 ± 102	735 ± 114
$BandwidthL$	606 ± 106	768 ± 129	694 ± 149	701 ± 139

For the raw data, the center frequency for R-ACA was found to be statistically higher in the female group than in the male group ($p = 0.02$). Additionally, significant difference was found between males and females in bandwidth on both channels (R-ACA: $p < 0.01$; L-ACA: $p = 0.01$). Considering that two out of three left-handed subjects are females, we reconsidered the left-handed group with right-handed-females and found out that no handedness effect could be concluded so far ($p > 0.05$).

5.4 TIME-FREQUENCY FEATURE

The relative energy calculated based on the 10-level wavelet decomposition and the wavelet entropy are summarized and presented in Tables 5.8-5.11. When considering the gender effect, no statistical difference could be found just by investigating the envelope (Tables 5.8 and 5.9). However, statistical difference can be found by looking at the raw signals.

The features for the raw data are summarized in Tables 5.10 and 5.11. There were gender-based difference in left channel entropy ($p = 0.01$). On the right channel, the detail coefficients d_{10}, d_9 and d_7 are shown to have gender-based difference ($p = 0.01, 0.04$ and 0.04 respectively). On the left channel, statistical difference was found in a_{10} ($p = 0.22$) and

Table 5.8: Time-frequency feature for the R-ACA envelope signals.

	Male	Female	Right-handed	Left-handed
WER	0.51 ± 0.19	0.49 ± 0.16	0.48 ± 0.18	0.59 ± 0.08
$E_{a_{10}}$	93.5 ± 3.05	93.9 ± 2.53	93.9 ± 2.89	92.3 ± 1.39
$E_{d_{10}}$	0.75 ± 0.63	0.85 ± 0.55	0.73 ± 0.58	1.24 ± 0.42
E_{d_9}	1.43 ± 1.21	1.60 ± 1.04	1.38 ± 1.12	2.30 ± 0.77
E_{d_8}	1.03 ± 0.84	1.12 ± 0.70	0.99 ± 0.77	1.61 ± 0.49
E_{d_7}	0.78 ± 0.41	0.77 ± 0.34	0.74 ± 0.39	0.96 ± 0.16
E_{d_6}	0.91 ± 0.29	0.59 ± 0.27	0.74 ± 0.32	0.72 ± 0.24
E_{d_5}	0.85 ± 0.26	0.71 ± 0.38	0.82 ± 0.33	0.53 ± 0.28
E_{d_4}	0.57 ± 0.53	0.34 ± 0.32	0.49 ± 0.47	0.17 ± 0.01
E_{d_3}	0.04 ± 0.03	0.05 ± 0.03	0.04 ± 0.03	0.07 ± 0.01
E_{d_2}	0.05 ± 0.03	0.03 ± 0.02	0.04 ± 0.03	0.05 ± 0.01
E_{d_1}	0.05 ± 0.04	0.04 ± 0.01	0.04 ± 0.03	0.03 ± 0.01

d_{10} ($p = 0.01$).Besides, when comparing the left-handed and the right-handed subjects, no statistical difference was found ($p > 0.08$ for all levels). This finding is the same as what we find in other extracted features, no statistical difference between the left-handed group and the right-handed group could be concluded.

Table 5.9: Time-frequency feature for the L-ACA envelope signals.

	Male	Female	Right-handed	Left-handed
WEL	0.44 ± 0.11	0.55 ± 0.18	0.49 ± 0.16	0.53 ± 0.15
$E_{a_{10}}$	94.7 ± 1.73	92.9 ± 2.89	93.8 ± 2.59	93.2 ± 2.54
$E_{d_{10}}$	0.55 ± 0.38	1.06 ± 0.61	0.79 ± 0.56	1.04 ± 0.64
E_{d_9}	1.03 ± 0.72	2.00 ± 1.14	1.50 ± 1.05	1.93 ± 1.18
E_{d_8}	0.76 ± 0.47	1.41 ± 0.77	1.07 ± 0.71	1.37 ± 0.76
E_{d_7}	0.71 ± 0.28	0.91 ± 0.38	0.81 ± 0.36	0.87 ± 0.30
E_{d_6}	0.88 ± 0.36	0.62 ± 0.29	0.75 ± 0.37	0.67 ± 0.16
E_{d_5}	0.81 ± 0.34	0.62 ± 0.23	0.72 ± 0.29	0.58 ± 0.30
E_{d_4}	0.40 ± 0.33	0.35 ± 0.33	0.40 ± 0.35	0.20 ± 0.06
E_{d_3}	0.04 ± 0.02	0.06 ± 0.04	0.05 ± 0.04	0.05 ± 0.02
E_{d_2}	0.04 ± 0.02	0.04 ± 0.02	0.04 ± 0.02	0.04 ± 0.02
E_{d_1}	0.06 ± 0.06	0.04 ± 0.02	0.05 ± 0.05	0.04 ± 0.02

Table 5.10: A summary of time-frequency features for the R-ACA raw signals.

	Male	Female	Right-handed	Left-handed
WER	1.94 ± 0.17	2.07 ± 0.18	1.96 ± 0.13	2.09 ± 0.05
$E_{a_{10}}$	0.02 ± 0.01	0.01 ± 0.01	0.01 ± 0.01	0.03 ± 0.01
$E_{d_{10}}$	6.55 ± 2.66	11.7 ± 4.64	9.02 ± 4.37	12.2 ± 5.64
E_{d_9}	15.6 ± 12.9	24.4 ± 9.83	20.5 ± 13.5	20.2 ± 2.26
E_{d_8}	38.2 ± 10.7	37.9 ± 6.48	37.5 ± 9.53	41.2 ± 1.62
E_{d_7}	31.8 ± 11.9	20.2 ± 9.61	26.7 ± 12.9	21.7 ± 5.84
E_{d_6}	6.41 ± 5.69	3.38 ± 1.32	5.22 ± 4.59	2.78 ± 0.73
E_{d_5}	0.82 ± 0.69	1.27 ± 2.54	0.61 ± 0.51	0.76 ± 0.84
E_{d_4}	0.35 ± 0.48	0.80 ± 1.89	0.21 ± 0.21	0.59 ± 0.70
E_{d_3}	0.18 ± 0.24	0.32 ± 0.61	0.12 ± 0.12	0.34 ± 0.28
E_{d_2}	0.13 ± 0.17	0.12 ± 0.19	0.07 ± 0.12	0.19 ± 0.12
E_{d_1}	0.03 ± 0.04	0.04 ± 0.05	0.02 ± 0.02	0.08 ± 0.05

Table 5.11: A summary of time-frequency features for the L-ACA raw signals.

	Male	Female	Right-handed	Left-handed
WEL	1.93 ± 0.12	2.16 ± 0.22	2.04 ± 0.16	1.98 ± 0.15
$E_{a_{10}}$	0.02 ± 0.01	0.01 ± 0.01	0.01 ± 0.01	$(6.99 \pm 3.04)^*$
$E_{d_{10}}$	6.15 ± 3.63	12.3 ± 5.82	9.41 ± 5.81	11.0 ± 6.34
E_{d_9}	15.3 ± 9.47	21.5 ± 7.80	8.34 ± 9.69	21.3 ± 6.68
E_{d_8}	39.9 ± 7.09	6.16 ± 5.82	37.4 ± 6.68	41.4 ± 6.52
E_{d_7}	30.7 ± 12.6	20.9 ± 8.70	27.1 ± 11.4	20.9 ± 9.95
E_{d_6}	6.31 ± 4.21	5.84 ± 3.55	6.30 ± 3.85	4.61 ± 4.29
E_{d_5}	0.85 ± 0.70	1.89 ± 3.68	0.83 ± 0.61	0.63 ± 0.63
E_{d_4}	0.42 ± 0.50	0.99 ± 2.59	0.33 ± 0.40	0.11 ± 0.06
E_{d_3}	0.18 ± 0.17	0.30 ± 0.68	0.15 ± 0.13	0.06 ± 0.03
E_{d_2}	0.07 ± 0.04	0.09 ± 0.15	0.06 ± 0.04	0.03 ± 0.02
E_{d_1}	0.02 ± 0.02	0.03 ± 0.04	0.02 ± 0.01	0.01 ± 0.01

6.0 DISCUSSION

In this chapter, we discuss the effects of gender and handedness on the extracted features from both the raw and envelope CBFV signals.

6.1 GENDER AND HANDEDNESS EFFECT

In the previous section, no evidence has been found of any handedness effect on CBFV in ACA, while gender-based differences were discovered.

The statistical analysis of the signals yielded several important results. Firstly, the difference in the the shape of the probability density function between males and females were discovered by comparing the calculated values of skewness and kurtosis. This finding demonstrates the significance of envelope signals from a statistical point of view. We can see that the envelope signals solely provide sufficient confidence in distinguishing males and females. Secondly, the maximum cross-correlation between the left channel and the right channel is close to 0 for the raw signals, implying that the signals obtained from two channels have low dependence in the time domain. On the contrary, the maximum cross-correlation coefficient value of the envelope signals is high, implying that the envelope signals have a high similarity at zero-lag between the two channels in time domain. However, none of these obtained features is found to exhibit any handedness effect.

From the information-theoretic point of view, the results show that the amount of information is not affected by gender or handedness. Interestingly, the envelope signals have almost the same Lempel-Ziv complexity as the raw signal. However, the envelope signals have a low regularity index (close to 0), while the raw signals have a higher regularity value. This means that the raw signals are more predictable than the envelope signals.

In the frequency analysis, the raw signals contain higher frequency components than do the envelope signals. In fact, the time domain features of the envelope signal already reflects some frequency domain characteristics because the the calculation that yields envelope signals involves Fourier transform [13]. However, the frequency analysis quantifies several parametric values in the frequency domain, while the time domain analysis of the envelope signal only provides a simple summary about the shape of the probability density function. Also, more specific features were found in the frequency analysis. Firstly, the envelope signals have a low-pass characteristic while the raw signals have a band-pass characteristic. Secondly, we noticed that large standard deviation values were obtained for the peak frequency feature when considering the envelope signals. This implies that the peak frequency of the envelope signals is not necessarily the most robust feature of these signals. Fortunately, the raw signal has a relatively more concentrated peak frequency statistic for both females and males. Additionally, the seeming differences between left-handed and right-handed subjects were found to be resulted from the gender effect rather than the handedness effect. That is to say, although gender effect has been clearly found out, handedness was not an obvious parameter that contributes to the frequency domain differences. On the other hand, the low-pass characteristic of the envelope signal is more likely to be contaminated by other physiological artifacts and the raw data avoids this disadvantage.

The time-frequency analysis has further demonstrated the existence of gender-based difference. Some of the detail coefficients calculated from the raw signal have shown significant difference between males and females. Comparatively, the envelope signal only shows that about 93% energy are concentrated around the approximate coefficient, i.e., the low frequency band. Otherwise, no handedness effect was found.

6.2 UTILIZATION OF RAW DATA AND ACA SIGNALS

Instead of only considering the envelope signal or the mean BFV, we also directly used the raw data to characterize the TCD measurements. This will be particularly important in future studies when cerebral blood flow during cognitive tasks is considered. In this study, we established the resting-state characterization using both the envelope and raw signals. Our study has shown that the raw data contains information that we could not capture by simply looking at the envelope signals.

Despite that the MCA was insonated in most of the related studies, we hope to characterize the cerebral blood flow using the ACA in addition to the MCA. Comparing with our previous MCA study [27], we have found out that in the frequency domain, the bandwidth of the ACA signals is larger than that of the MCA signals. The ACA has $\approx$ 13 Hz in envelope signals and $\approx$ 600 Hz in raw signals, while the MCA has $\approx$ 10 Hz in envelope signals and $\approx$ 500 Hz in raw signals. Bandwidth difference between the ACA and the MCA indicates different cut-off frequencies and hence represents different frequency response characteristics. In the time-frequency domain, the wavelet entropy calculation is also found to be presenting statistical difference. MCA has wavelet entropy at 1.77 ± 0.17 [27], and ACA has 1.94 ± 0.16. This finding demonstrates a different energy spreadness over different levels. On the other hand, there also exists consistency in our current ACA study and the previous MCA study. Firstly, in both the MCA and the ACA analysis, the time domain features of envelope and raw signals have exhibited similar results in kurtosis, skewness and cross-correlation. This demonstrates the similarity between the shapes of the probability density function considered in the ACA and the MCA. Secondly, in the frequency domain, the MCA and the ACA have similar findings in peak and centroid frequencies. Lastly, in the time-frequency domain, when considering the raw signal, most energy concentrates around the 8th level and spreads over neighboring levels in both the ACA and the MCA.

7.0 CONCLUSIONS AND FUTURE WORK

7.1 CONCLUSIONS

In this thesis, we investigated the resting-state characteristics of cerebral blood flow through anterior cerebral arteries using the transcranial Doppler recordings. We collected data from 20 healthy participants during a 15-minute resting period. Both the envelope signals and the raw TCD signals were considered. The acquired data was analyzed in time, frequency and time-frequency domain. The results of the numerical analysis showed several important trends. In the time domain, we have found that the envelope signals carries good amount of representative features in terms of the separation of males and females, and hence it is convenient to use envelope signal in this sense. In the information-theoretic analysis, the envelope signals and the raw signals are found to contain almost the same amount of information except the raw signals have higher synchronization. In the frequency domain, the envelope signals exhibited a low-pass characteristic, while the raw signals exhibited a band-pass characteristic. We may thus take advantage of the band-pass characteristic in the future to avoid other low-frequency physiological artifacts. Finally, the time-frequency features were extracted using 10-level Mayer discrete wavelet decomposition. They have shown that the energy of the envelope signals are concentrated on the low frequency band while the energy of the raw signals are more spread out in several bands. We have found statistical differences between males and females in the time, frequency and time-frequency domain. However, no handedness effect could be concluded.

7.2 FUTURE DIRECTIONS

Our current project focuses on the characterization of the resting state. However, the research goal is to understand the behavior of cerebral blood flow and study cognitive tasks. Furthermore, we wish to develop models that describe the relationship between simple human cognitive activities and cerebral blood flow change, and then design real-time implementation for a wide range of applications, i.e. BCI. The next step will involve geometrical tasks and word generation tasks. We will design algorithms to distinguish their different states. In addition to TCD measurements, other physiological parameters will be considered as well. The methodology might include pattern recognition and machine learning.

More specifically, I suggest raising the following questions to identify future work:

1. *Which features should be utilized to distinguish resting states and cognitive states?*
2. *Are the features we extracted sufficient to distinguish verbal task and geometric task?*
3. *Is the run time of the data processing and algorithm implementation short enough to satisfy the general requirement of building a BCI?*

By answering these questions, we will have a further understanding about the feasibility of TCD-based BCI using the raw signal.

Alternatively, we may proceed along another research track to optimize our BCI design in the future. Time-frequency distribution analysis [57] may provide a valuable insight into the signal characteristics by considering time-frequency based statistical features. In doing so, we hope to loosen the strict assumption that the signals are stationary and their moments are constants. Under the circumstances, we might investigate the raw data and seek mathematical modeling of its non-stationarity [58] .

BIBLIOGRAPHY

[1] K. Tai, S. Blain, and T. Chau, "A review of emerging access technologies for individuals with severe motor impairments," *Assistive Technology*, vol. 20, no. 4, pp. 204–221, 2008.

[2] N. Birbaumer, "Breaking the silence: brain–computer interfaces (BCI) for communication and motor control," *Psychophysiology*, vol. 43, no. 6, pp. 517–532, 2006.

[3] N. Weiskopf, K. Mathiak, S. W. Bock, F. Scharnowski, R. Veit, W. Grodd, R. Goebel, and N. Birbaumer, "Principles of a brain-computer interface (BCI) based on real-time functional magnetic resonance imaging (fmri)," *IEEE Transactions on Biomedical Engineering*, vol. 51, no. 6, pp. 966–970, 2004.

[4] E. Smith and M. Delargy, "Locked-in syndrome," *BMJ*, vol. 330, no. 7488, pp. 406–409, 2005.

[5] B. Wilhelm, M. Jordan, and N. Birbaumer, "Communication in locked-in syndrome: effects of imagery on salivary ph," *Neurology*, vol. 67, no. 3, pp. 534–535, 2006.

[6] B. Allison, E. Wolpaw, and J. Wolpaw, "Brain–computer interface systems: progress and prospects," *Expert Review of Medical Devices*, vol. 4, no. 4, pp. 463–474, 2007.

[7] H. Ayaz, P. Shewokis, S. Bunce, M. Schultheis, and B. Onaral, "Assessment of cognitive neural correlates for a functional near infrared-based brain computer interface system," *Foundations of Augmented Cognition. Neuroergonomics and Operational Neuroscience*, pp. 699–708, 2009.

[8] M. Van Gerven, J. Farquhar, R. Schaefer, R. Vlek, J. Geuze, A. Nijholt, N. Ramsey, P. Haselager, L. Vuurpijl, S. Gielen *et al.*, "The brain–computer interface cycle," *Journal of Neural Engineering*, vol. 6, no. 4, pp. 041 001–1–10, 2009.

[9] B. Min, M. Marzelli, and S. Yoo, "Neuroimaging-based approaches in the brain-computer interface," *Trends in Biotechnology*, vol. 28, no. 11, pp. 552–560, 2010.

[10] P. Fransson, "Spontaneous low-frequency BOLD signal fluctuations: An fMRI investigation of the resting-state default mode of brain function hypothesis," *Human Brain Mapping*, vol. 26, no. 1, pp. 15–29, 2005.

[11] M. Phelps, J. Mazziotta *et al.*, "Positron emission tomography: Human brain function and biochemistry." *Science*, vol. 228, no. 4701, p. 799, 1985.

[12] N. Stroobant and G. Vingerhoets, "Transcranial Doppler ultrasonography monitoring of cerebral hemodynamics during performance of cognitive tasks: a review," *Neuropsychology Review*, vol. 10, no. 4, pp. 213–231, 2000.

[13] M. Deppe, E. Ringelstein, and S. Knecht, "The investigation of functional brain lateralization by transcranial Doppler sonography," *NeuroImage*, vol. 21, no. 3, pp. 1124–1146, 2004.

[14] R. Aaslid, T. Markwalder, and H. Nornes, "Noninvasive transcranial Doppler ultrasound recording of flow velocity in basal cerebral arteries," *Journal of Neurosurgery*, vol. 57, no. 6, pp. 769–774, 1982.

[15] P. Fox and M. Raichle, "Focal physiological uncoupling of cerebral blood flow and oxidative metabolism during somatosensory stimulation in human subjects," *Proceedings of the National Academy of Sciences*, vol. 83, no. 4, pp. 1140–1144, 1986.

[16] M. Matteis, E. Troisi, B. Monaldo, C. Caltagirone, and M. Silvestrini, "Age and sex differences in Cerebral Hemodynamics: a transcranial Doppler Study," *Stroke*, vol. 29, no. 5, pp. 963–967, 1998.

[17] M. Marinoni, A. Ginanneschi, D. Inzitari, S. Mugnai, and L. Amaducci, "Sex-related differences in human cerebral hemodynamics," *Acta Neurologica Scandinavica*, vol. 97, no. 5, pp. 324–327, 2009.

[18] M. Torbey, T. Hauser, A. Bhardwaj, M. Williams, J. Ulatowski, M. Mirski, and A. Razumovsky, "Effect of age on cerebral blood flow velocity and incidence of vasospasm after aneurysmal subarachnoid hemorrhage," *Stroke*, vol. 32, no. 9, pp. 2005–2011, 2001.

[19] X. Ducrocq, W. Hassler, K. Moritake, D. Newell, G. von Reutern, T. Shiogai, and R. Smith, "Consensus opinion on diagnosis of cerebral circulatory arrest using Doppler-sonography: Task Force Group on cerebral death of the Neurosonolgy Research Group of the World Federation of Neurology," *Journal of the Neurological Sciences*, vol. 159, no. 2, pp. 145–150, 1998.

[20] A. Myrden, A. Kushki, E. Sejdić, A. Guerguerian, and T. Chau, "A brain-computer interface based on bilateral transcranial doppler ultrasound," *PloS ONE*, vol. 6, no. 9, p. e24170, 2011.

[21] A. Myrden, A. Kushki, E. Sejdić, and T. Chau, "Towards increased data transmission rate for a three-class metabolic brain-computer interface based on transcranial Doppler ultrasound," *Neuroscience Letters*, vol. 528, no. 2, pp. 99–103, 2012.

[22] H. Laufs, K. Krakow, P. Sterzer, E. Eger, A. Beyerle, A. Salek-Haddadi, and A. Kleinschmidt, "Electroencephalographic signatures of attentional and cognitive default modes

in spontaneous brain activity fluctuations at rest," *Proceedings of the National Academy of Sciences*, vol. 100, no. 19, pp. 11 053–11 058, 2003.

[23] O. Sporns, D. Chialvo, M. Kaiser, C. Hilgetag *et al.*, "Organization, development and function of complex brain networks," *Trends in Cognitive Sciences*, vol. 8, no. 9, pp. 418–425, 2004.

[24] R. Kelley, J. Chang, N. Scheinman, B. Levin, R. Duncan, and S. Lee, "Transcranial Doppler assessment of cerebral flow velocity during cognitive tasks," *Stroke*, vol. 23, no. 1, pp. 9–14, 1992.

[25] N. Stroobant, D. Buijs, and G. Vingerhoets, "Variation in brain lateralization during various language tasks: A functional transcranial Doppler study," *Behavioural Brain Research*, vol. 199, no. 2, pp. 190–196, 2009.

[26] S. Duschek and R. Schandry, "Functional transcranial Doppler sonography as a tool in psychophysiological research," *Psychophysiology*, vol. 40, no. 3, pp. 436–454, 2003.

[27] E. Sejdić, D. Kalika, and N. Czarnek, "An analysis of resting-state functional transcranial Doppler recordings from middle cerebral arteries," *PLoS ONE*, 2012, accepted.

[28] B. Carey, B. Manktelow, R. Panerai, and J. Potter, "Cerebral autoregulatory responses to head-up tilt in normal subjects and patients with recurrent vasovagal syncope," *Circulation*, vol. 104, no. 8, pp. 898–902, 2001.

[29] D. Droste, A. Harders, and E. Rastogi, "A transcranial doppler study of blood flow velocity in the middle cerebral arteries performed at rest and during mental activities," *Stroke*, vol. 20, no. 8, pp. 1005–1011, 1989.

[30] W. Hartje, E. Ringelstein, B. Kistinger, D. Fabianek, and K. Willmes, "Transcranial doppler ultrasonic assessment of middle cerebral artery blood flow velocity changes during verbal and visuospatial cognitive tasks," *Neuropsychologia*, vol. 32, no. 12, pp. 1443–1452, 1994.

[31] H. Gibo, C. Carver, A. Rhoton Jr, C. Lenkey, and R. Mitchell, "Microsurgical anatomy of the middle cerebral artery," *Journal of Neurosurgery*, vol. 54, no. 2, pp. 151–169, 1981.

[32] H. White and B. Venkatesh, "Applications of transcranial Doppler in the ICU: a review," *Intensive Care Medicine*, vol. 32, no. 7, pp. 981–994, 2006.

[33] G. Bradac, "Anterior Cerebral Artery," *Cerebral Angiography*, pp. 47–56, 2011.

[34] E. Ross, "Left medial parietal lobe and receptive language functions mixed transcortical aphasia after left antmior cerebral artery infarction," *Neurology*, vol. 30, no. 2, pp. 144–144, 1980.

[35] M. Alexander, D. Benson, and D. Stuss, "Frontal lobes and language," *Brain and Language*, vol. 37, no. 4, pp. 656–691, 1989.

[36] A. Wagner, B. Shannon, I. Kahn, and R. Buckner, "Parietal lobe contributions to episodic memory retrieval," *Trends in Cognitive Sciences*, vol. 9, no. 9, pp. 445–453, 2005.

[37] H. Azhari, *Basics of biomedical ultrasound for engineers*. Wiley-IEEE Press, 2010.

[38] A. Papoulis and R. Probability, *Stochastic processes*. McGraw-hill New York, 1991, vol. 3.

[39] R. W. Gill, "Measurement of blood flow by ultrasound: accuracy and sources of error," *Ultrasound in Medicine and Biology*, vol. 11, no. 4, pp. 625–641, 1985.

[40] R. Oldfield, "The assessment and analysis of handedness: the Edinburgh inventory," *Neuropsychologia*, vol. 9, no. 1, pp. 97–113, 1971.

[41] S. Piechnik, X. Yang, M. Czosnyka, P. Smielewski, S. Fletcher, A. Jones, and J. Pickard, "The continuous assessment of cerebrovascular reactivity: a validation of the method in healthy volunteers," *Anesthesia & Analgesia*, vol. 89, no. 4, pp. 944–944, 1999.

[42] P. Chauvy, C. Madore, and D. Landolt, "Variable length scale analysis of surface topography: characterization of titanium surfaces for biomedical applications," *Surface and Coatings Technology*, vol. 110, no. 1, pp. 48–56, 1998.

[43] J. J. Christopher and W. H. Christian, "Independent component analysis for biomedical signals," *Physiological Measurement*, vol. 26, no. 1, p. R15, 2005.

[44] M. Aboy, R. Hornero, D. Abasolo, and D. Alvarez, "Interpretation of the Lempel-Ziv complexity measure in the context of biomedical signal analysis," *IEEE Transactions on Biomedical Engineering*, vol. 53, no. 11, pp. 2282 –2288, 2006.

[45] A. Porta, S. Guzzetti, N. Montano, M. Pagani, V. Somers, A. Malliani, G. Baselli, and S. Cerutti, "Information domain analysis of cardiovascular variability signals: evaluation of regularity, synchronisation and co-ordination," *Medical and Biological Engineering and Computing*, vol. 38, no. 2, pp. 180–188, 2000.

[46] J. Hu, J. Gao, and J. Principe, "Analysis of biomedical signals by the Lempel-Ziv complexity: the effect of finite data size," *IEEE Transactions on Biomedical Engineering*, vol. 53, no. 12, pp. 2606–2609, 2006.

[47] R. Coifman and M. Wickerhauser, "Entropy-based algorithms for best basis selection," *IEEE Transactions on Information Theory*, vol. 38, no. 2, pp. 713–718, 1992.

[48] E. Sejdić, C. Steele, and T. Chau, "The effects of head movement on dual-axis cervical accelerometry signals," *BMC Research Notes*, vol. 3, no. 1, p. 269, 2010.

[49] Y. Quan and J. Harris, "Seismic attenuation tomography using the frequency shift method," *Geophysics*, vol. 62, no. 3, pp. 895–905, 1997.

[50] S. Li, "Content-based audio classification and retrieval using the nearest feature line method," *IEEE Transactions on Speech and Audio Processing*, vol. 8, no. 5, pp. 619–625, 2000.

[51] C. S. Burrus, R. A. Gopinath, and H. Guo, *Introduction to wavelets and wavelet transforms: a primer*. Upper Saddle River, NJ: Prentice Hall, 1998.

[52] O. Rosso, S. Blanco, J. Yordanova, V. Kolev, A. Figliola, M. Schurmann, and E. Basar, "Wavelet entropy: a new tool for analysis of short duration brain electrical signals," *Journal of Neuroscience Methods*, vol. 105, no. 1, pp. 65–76, 2001.

[53] J. Lee, E. Sejdić, C. Steele, and T. Chau, "Effects of liquid stimuli on dual-axis swallowing accelerometry signals in a healthy population," *Biomedical Engineering Online*, vol. 9, no. 1, p. 7, 2010.

[54] M. Bračič and A. Stefanovska, "Wavelet-based analysis of human blood-flow dynamics," *Bulletin of Mathematical Biology*, vol. 60, no. 5, pp. 919–935, 1998.

[55] V. DePuy, V. Berger, and Y. Zhou, "Wilcoxon–Mann–Whitney Test," *Encyclopedia of Statistics in Behavioral Science*, 2005.

[56] C. Giller, G. Bowman, H. Dyer, L. Mootz, and W. Krippner, "Cerebral arterial diameters during changes in blood pressure and carbon dioxide during craniotomy," *Neurosurgery*, vol. 32, no. 5, pp. 737–742, 1993.

[57] L. Cohen, "Time-frequency distributions-a review," *Proceedings of the IEEE*, vol. 77, no. 7, pp. 941–981, 1989.

[58] K. F. K. Wong, A. Galka, O. Yamashita, and T. Ozaki, "Modelling non-stationary variance in eeg time series by state space garch model," *Computers in Biology and Medicine*, vol. 36, no. 12, pp. 1327–1335, 2006.